Article

Transient Kinetic QXAFS Approach for Understanding the RDE−MEA Gap in Fuel Cell (Oxygen Reduction Reaction) Performances of Pt-Based Electrocatalysts

Takefumi Yoshida,[∇] Shinobu Takao,[∇] Hiroko Ariga-Miwa,[∇] Xiao Zhao, Gabor Samjeské,
Takuma Kaneko, Tomoya Uruga, and Yasuhiro Iwasawa*

Read Online

ACCESS | Metrics & More | Article Recommendations | Supporting Information

ABSTRACT: There is a large gap between the performances indicated by rotating disk electrode (RDE) results in acidic media and the actual performances obtained in membrane-electrode assemblies (MEAs) composed of the same electrocatalysts. It is unclear whether the intrinsic kinetic reactivity of the available surface Pt sites of Pt-based cathode electrocatalysts is similar or different at RDE and in MEA. To address this, we used an operando element-selective time-resolved Pt L_{III}-edge quick X-ray absorption fine structure (QXAFS) technique to determine transient response profiles and rate constants, $k_{d(WL)}$, $k_{d(CN_{Pt-O})}$, and $k_{d(CN_{Pt-Pt})}$, corresponding to changes in the oxidation states [white line (WL) intensity] and local structures (coordination numbers of Pt−O and Pt−Pt bonds) at Pt sites for nine representative Pt-based cathode electrocatalysts under transient voltage operations, aiming to understand the oxygen reduction reaction (ORR) performance gap between RDE and MEA. For

the first time, the transient kinetics and reactivity of electrocatalyst themselves in MEA, characterized by the operando QXAFS analysis technique, were systematically compared with the electrochemical activity [mass activity (I_{mass}) and surface specific activity ($I_{specific}$)] of the electrocatalysts in MEA and at RDE. The operando time-resolved QXAFS analysis revealed that the ORR activities of available surface Pt sites at RDEs of the electrocatalysts, including notably structured electrocatalysts (concave octahedral $PtNi_x/C$ and Pt nanowire/C), were kinetically reflected at good levels of $k_{d(WL)}$ and $k_{d(CN_{Pt-O})}$ in MEA performances, despite large RDE−MEA gaps observed in the electrochemically determined I_{mass} and $I_{specific}$. As the I_{mass} and $I_{specific}$ of MEA increased, the relaxation time $k_{d(CN_{Pt-Pt})}^{-1}$, which indicates long-term durability, decreased, reflecting a dilemma in the development of remarkable Pt-based electrocatalysts, while the $k_{d(CN_{Pt-Pt})}^{-1}$ was almost independent of ECSA. The differences and similarities in the kinetic reactivity and durability of the Pt surface between RDE and MEA were examined using operando QXAFS transient kinetics and electrochemical performance measurements to elucidate the underlying factors contributing to the performance gap between RDE and MEA. The insights gained aim to support the development of next-generation polymer electrolyte fuel cells with enhanced performance and durability by leveraging the operando time-resolved QXAFS technique under the transient kinetic-response operation.
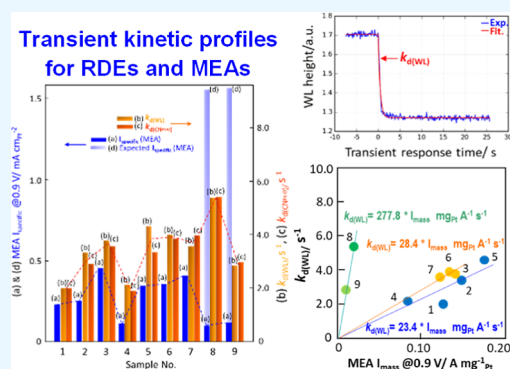
INTRODUCTION

Battery electric, plug-in hybrid, and hydrogen fuel cell vehicles have already been commercialized. However, these technologies are still undergoing further development in many countries, and the future roles of each in transportation systems are currently a topic of debate.[1] Nevertheless, polymer electrolyte fuel cells (PEFCs), which convert hydrogen to electricity, have received significant attention as one of the most efficient clean energy generation systems. PEFCs are poised to play a vital role in a carbon-neutral, sustainable society, particularly for heavy-duty vehicles, passenger vehicles, trains, ships, forklifts, etc. A major obstacle in advancing fuel cell technology is the sluggish kinetics of oxygen reduction reactions (ORRs) on cathode electrocatalysts.[2] The current status of the efficiency, performance, and

long-term durability of membrane-electrode assembly (MEA), a core component in PEFC, still falls short of the targets necessary for widespread commercialization in transportation.

Various strategies have been employed to develop highly active electrocatalysts, and over the past decades, substantial progress has been reported in enhancing ORR activities at rotating disk electrodes (RDEs) in acidic media.[3−15] Platinum-

based materials remain the primary catalysts used in the PEFCs. Despite advancements in synthesizing diverse cathode electrocatalysts for RDEs, the practical MEAs fabricated from these electrocatalysts often do not achieve the anticipated efficiency, performance, and durability.[2,5,16−21] The mass activity (I_{mass}) and surface specific activity ($I_{specific}$) measured at RDEs are generally larger than those measured in MEAs due to the more complex environment in MEAs compared to that in RDEs (Figure S1). Consequently, the highest-performing RDE systems are not yet practical for PEFC applications.[2] It is suggested that Pt catalytic sites in the MEA cathode layer are not fully utilized as ORR sites, primarily due to high mass transport resistance caused by undesired ionomer distribution on Pt surfaces.[21,22] Additionally, the MEA catalyst layer typically consists of non-uniform aggregates of ionomer, Pt/C catalyst, and carbon pores, leading to heterogeneous distribution of catalysts that are either fully covered with ionomer films or have little to no ionomer coverage.[23−25] Proton transport is impeded when the ionomer is absent on the catalyst surface.

Few catalysts with remarkable activities have been successfully integrated into the MEA stacking configuration, and a significant discrepancy exists between the performances reported by RDE results in acidic media and the actual performances achieved in MEAs utilizing the same electrocatalysts. It remains unclear whether the intrinsic kinetic reactivity of the available surface Pt sites of Pt-based cathode electrocatalysts is consistent or differs between the RDE and MEA measurements. This uncertainty is due to a lack of direct measurements of the reactivity and structural kinetics of available active Pt sites in MEA as MEA performances are typically assessed by evaluating the overall current−voltage characteristics of PEFCs. To address this issue, we utilized a transient kinetic quick X-ray absorption fine structure (QXAFS) approach to study MEA cathode electrocatalysis, aiming to understand the ORR performance gap between RDE and MEA. The structural kinetics at Pt-based nanoparticle surfaces in MEA, determined using the transient technique, can be compared with electrochemical I_{mass} and $I_{specific}$ values obtained from RDE measurements.

Time-resolved QXAFS enables operando element-selective characterization to determine transient response profiles and rate constants, $k_{d(WL)}$, $k_{d(CN_{Pt-O})}$, and $k_{d(CN_{Pt-Pt})}$, corresponding to changes in the oxidation states and local structures (CN_{Pt-O} and CN_{Pt-Pt}; CN: coordination number) at active Pt sites in MEA under voltage operating conditions (Figure S2).[26−29] Tada et al. reported a linear relationship between the ORR performances of MEA Pt/C, Pt₃Co/C, and Pt₃Ni/C cathode electrocatalysts and the rate constants $k_{d(WL)}$ and $k_{d(CN_{Pt-O})}$ under the transient voltage operations.[30] Using MEAs with Pt/C (different kinds of carbons), we also identified correlations between the ORR performances of the MEA Pt/C electrocatalysts and the rate constants $k_{d(WL)}$ and $k_{d(CN_{Pt-O})}$, as well as between the MEA durability and the inverse rate constant $k_{d(CN_{Pt-Pt})}^{-1}$ for the transformation of CN_{Pt-Pt}, as determined by operando time-resolved QXAFS (Figure S3).[31]

In this study, we first report the ORR performance gap between RDEs and PEFC-MEAs using nine representative Pt-based electrocatalysts with varying types and performances. Second, we report the structural kinetics and rate constants [$k_{d(WL)}$, $k_{d(CN_{Pt-O})}$, and $k_{d(CN_{Pt-Pt})}$] for the nine representative Pt-based cathode electrocatalysis in MEAs under transient voltage operations, determined by the operando element-selective time-resolved Pt L_{III}-edge QXAFS spectroscopic technique. Third, we establish a linear relationship between the electrochemical characteristics [electrochemically active surface area (ECSA), I_{mass}, and $I_{specific}$] of the electrocatalysts at the RDE and the reaction kinetics [$k_{d(WL)}$, $k_{d(CN_{Pt-O})}$, and $k_{d(CN_{Pt-Pt})}^{-1}$] of the electrocatalysis at the cathode in MEA during voltage transient response processes. The differences and similarities in Pt surface reactivity between RDE and MEA are discussed from the perspective of the transient reaction kinetics of available Pt sites (catalyst activity itself) to elucidate the cause of the RDE-MEA performance gap.

■ RESULTS AND DISCUSSION

Cyclic Voltammograms (CVs), $I−V$ Polarization Curves, and Power Densities for MEA Cathode Electrocatalysts. We have characterized the electrochemical properties, including ECSA, I_{mass}, $I_{specific}$, and power density, of nine representative MEA cathode electrocatalysts. CVs and $I−V$ polarization curves for MEA cathode electrocatalysts were measured in the MEA-mounted operando PEFC XAFS cell (Figure S1) at 353 K, while measuring XAFS spectra, in a similar manner to those previously reported.[28−35] The electrochemical measurements of MEA in PEFC are described in the Experimental Section and the Supporting Information in more detail. Figure 1a,b presents CVs of typical spherical and structured electrocatalysts among the examined MEA cathode electrocatalysts. Specifically, Figure 1a shows the CVs for 50 wt % Pt/C (TEC10E50E: 0.63 mg_Pt cm⁻²) (black), 50 wt % Pt/C (TEC10E50E-HT: 0.62 mg_Pt cm⁻²) (blue), 30 wt % Pt/C (TEC10E30E: 0.61 mg_Pt cm⁻²) (green), and 20 wt % Pt nanowires (NW) /C (0.61 mg_Pt cm⁻²) (yellow). Figure 1b depicts the CVs for concave octahedral PtNi_x (Pt₇₃Ni₂₇)/C in MEA (16.0 wt %; 0.21 mg_Pt cm⁻² and 19.1 wt %; 0.62 mg_Pt cm⁻²). The morphologies of the reference Pt/C (TEC10E50E) cathode electrocatalyst, as-synthesized Pt NWs, carbon-supported Pt single NW, and concave octahedral PtNi_x nanoparticles are imaged by TEM/STEM in Figure 1c, d-1, d-2, and e, respectively. Figure 1f shows $I−V$ polarization curves and power densities for concave octahedral PtNi_x/C (red: 1) and Pt₃Ni/C (TECNi52) (purple: 2) in MEA at 353 K. Figure 1g exhibits $I−V$ polarization curves and power densities for various MEA Pt/C samples: Pt/C (TEC10E50E) (black: 3), Pt/C (TEC10E30NC) (green: 4), Pt/C (TEC10E50E-HT) (blue: 5), and Pt NW/C (yellow: 6). The I_{mass} (current per mg-Pt) and $I_{specific}$ (current per cm²-Pt) values of the MEA cathodes were calculated from the kinetic activities at 0.9 V, where mass transport loss is negligible. These values were evaluated using semilogarithmic plots (Tafel plots) of $I−V$ polarization curves in H₂ (anode) and air (cathode) environments.[35] A typical example for the concave octahedral PtNi_x/C (19.1 wt % Pt; 0.62 mg_Pt cm⁻²) in MEA is shown in the inset of Figure 1f and in Figure S4.

RDE−MEA Gap in ORR Kinetic Activities. Figure 2 compares the ORR kinetic activities (I_{mass} and $I_{specific}$) at 0.90 V for nine representative electrocatalysts (1−9) at RDE and in MEA: Pt/C (TEC10E50E) (1 and 2), Pt/C (TEC10E50E-HT) (3), Pt/C (TEC10E30E) (4), Pt/C (TEC10E30NC) (5), Pt₃Ni/C (TECNi52) (6), Pt₃Co/C (TEC36E52) (7), concave octahedral PtNi_x/C (8), and Pt NW/C (9). In Figure 2, blue bars, yellow bars, and green bars represent samples with 2.5−2.8 nm nanoparticles, 4.5 nm nanoparticles, and structured nanoparticles (14.2 nm concave octahedron and 1.3 nm wire), respectively. The I_{mass} and $I_{specific}$ values for the electrocatalysts in
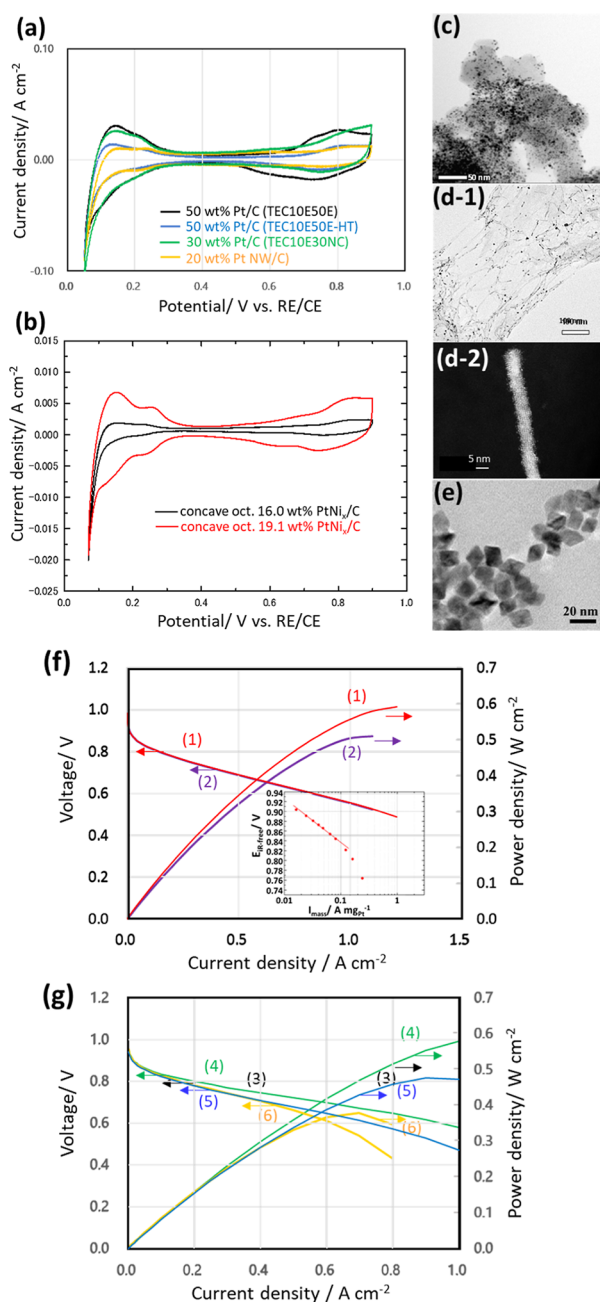
Figure 1. (a) Typical CVs of representative MEA Pt/C samples; Pt/C: 50 wt % Pt/C (TEC10E50E: 0.63 mg_{Pt} cm^{-2}) (black), 50 wt % Pt/C (TEC10E50E-HT: 0.62 mg_{Pt} cm^{-2}) (blue), 30 wt % Pt/C (TEC10E30E: 0.61 mg_{Pt} cm^{-2}) (green), and 20 wt % Pt NW-(nanowire)/C (0.61 mg_{Pt} cm^{-2}) (yellow). (b) CVs of concave octahedral $PtNi_x(Pt_{73}Ni_{27})$/C (16.0 wt %; 0.21 mg_{Pt} cm^{-2}) (black) and (19.1 wt %; 0.62 mg_{Pt} cm^{-2}) (red) in MEA. (c) TEM image of Pt/C (TEC10E50E) as a reference cathode electrocatalyst. (d-1) and (d-2) STEM images of as-synthesized Pt nanowires and carbon-supported Pt single nanowire, respectively. (e) TEM image of concave octahedral $PtNi_x$ nanoparticles (after ref 10). (f) $I−V$ polarization curves (V vs RHE) and power densities for MEA Pt−Ni/C samples; concave octahedral $PtNi_x$/C (red: 1) and Pt_3Ni/C (TECNi52) (purple: 2). Inserted figure: Tafel plot for the concave octahedral $PtNi_x$/C (19.1 wt % Pt; 0.62 mg_{Pt} cm^{-2}) in MEA as a typical example. (g) $I−V$ polarization curves and power densities for typical MEA Pt/C samples; Pt/C (TEC10E50E) (black: 3), Pt/C (TEC10E30NC) (green: 4), Pt/ C (TEC10E50E-HT) (blue: 5), and Pt NW/C (yellow: 6).

MEA were generally lower than those at RDE, except for the heat-treated Pt/C (TEC10E50E-HT), showing the significant discrepancy between the RDE performances in acidic media and the actual MEA performances utilizing the same electro-catalysts.[2,5,16−21] The RDE-MEA gap was notable for the structured electrocatalysts (8 and 9), which exhibited remarkable ORR activities at RDE but much lower activities in MEA, as shown in Figure 2. The $I_{specific}$ values of $PtNi_x$/C (8) and Pt NW/C (9) at RDE were 21.3 times and 11.6 times greater, respectively, than that of the standard Pt/C (TEC10E50E) (1 and 2) at RDE. However, in MEA, the $I_{specific}$ values of $PtNi_x$/C and Pt NW/C were approximately half (1/2.4 and 1/2.0, respectively) of that of the standard Pt/C. Further, the $I_{specific}$ of $PtNi_x$/C and Pt NW/C (5.33 and 2.90 mA cm_{Pt}^{-2}, respectively) at RDE significantly decreased to 0.097 and 0.116 mA cm_{Pt}^{-2} in MEA, corresponding to only 1.8 and 4.0% of the RDE values, respectively. As a result, among the examined samples (1−9), particularly, the practical MEAs fabricated from the structured electrocatalysts (8 and 9), which showed remarkable activities at RDE, did not achieve the anticipated efficiency and performance.

Relations between RDE and MEA in ECSA, I_{mass}, and $I_{specific}$. The relationships between the ORR kinetic activities (I_{mass} and $I_{specific}$) of Pt-based electrocatalysts (1−9) at RDE and in MEA are shown in Figure S5. The remarkable ORR kinetic activities of samples 8 and 9 at RDE are illustrated in the inset of Figure S5a. The data are categorized along three different lines (blue, yellow, and green) based on the ECSA and particle size at RDE (a) and MEA (b). A similar trend is also reported in the literature.[2]

Figure 3 presents the relationships between RDE ECSA and MEA ECSA (a) and between RDE kinetic activity and MEA kinetic activity at 0.9 V [I_{mass} (b) and $I_{specific}$ (c)]. The derived equations, $I_{specific}$ (MEA) = 0.77 × $I_{specific}$ (RDE) for samples (1, 2, 4, and 5), $I_{specific}$ (MEA) = 0.88 × $I_{specific}$ (RDE) for samples (3, 6, and 7), and $I_{specific}$ (MEA) = 0.033 × $I_{specific}$ (RDE) for samples (8 and 9) coincide with those calculated from I_{mass}/ECSA within the margin of experimental errors, which may justify that the RDE−MEA gap in I_{mass} and $I_{specific}$ is categorized along three different lines (blue, yellow, and green) in Figure 3b,c, though the data for the samples (1−7) are scattered. The electro-chemical experiments indicate that the structured electro-catalysts, concave octahedral $PtNi_x$/C (8) and Pt NW/C (9), followed entirely different trends from the samples (1−7) with roughly spherical shapes of 2.5−2.8 and 4.5 nm sizes, as shown in Figure 3b,c. Notably, the ECSAs of all samples (1−9) aligned on the same straight line (Figure 3a), whereas the electrochemical activities (I_{mass} and $I_{specific}$) of the structured electrocatalysts (8 and 9) in MEA did not correlate with their corresponding ORR activities at the RDE.

The significantly lower performances of the structured electrocatalysts (8 and 9) in MEA compared to the other electrocatalysts (1−7) may be attributed to poor utilization of available Pt surface sites in MEA. This could be caused by the undesired locations of catalytic nanoparticles within the carbon assemblies, oxygen transport and concentration depletion near the electrocatalyst surface, inadequate and insufficient catalyst/ionomer interaction, electrical resistance, and undesired poison by Nafion sulfonate moieties.[20,36−40] Moreover, it remains unexamined whether the kinetic reactivity and limitations of cathode nanoparticle surfaces in actual MEA are inherently lower than those at RDE in acidic media, which brings about an intrinsic decrease in the ORR kinetic performance of MEA. We
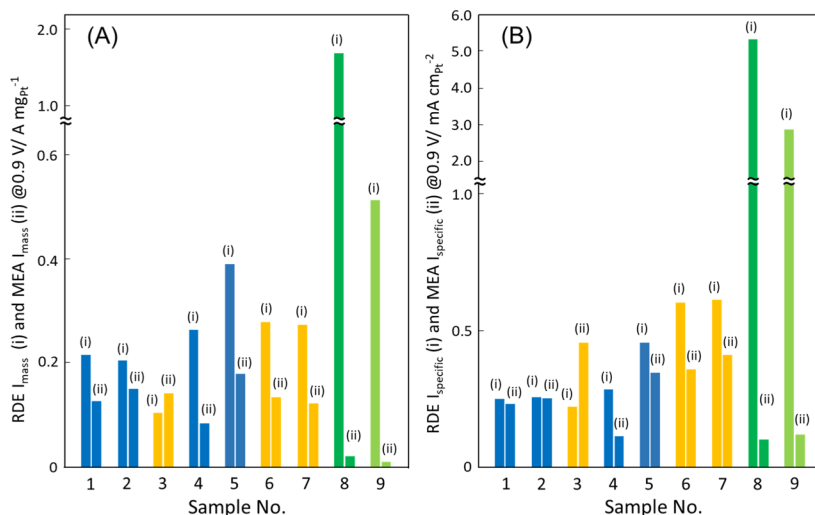
Figure 2. ORR kinetic activities [mass activities (A) and surface specific activities (B)] at 0.90 V for the samples 1−9 at RDE (i) and in MEA (ii). Voltage: vs RHE. Cathode electrocatalyst samples: (1 and 2) Pt/C (TEC10E50E), (3) Pt/C (TEC10E50E-HT), (4) Pt/C (TEC10E30E), (5) Pt/C (TEC10E30NC), (6) Pt$_3$Ni/C (TECNi52), (7) Pt$_3$Co/C (TEC36E52), (8) concave octahedral PtNi$_x$(Pt$_{73}$Ni$_{27}$)/C, and (9) Pt NW/C. Averaged nanoparticle sizes of the 1−9 electrocatalysts are 2.8 nm [1& 2: Pt/C (TEC10E50E), 4: Pt/C (TEC10E30E)], 2.5 nm [5: Pt/C (TEC10E30NC)], 4.5 nm [3: Pt/C (TEC10E50E-HT), 6: Pt$_3$Ni/C (TECNi52), 7: Pt$_3$Co/C (TEC36E52)], 14.2 nm [8: concave octahedral PtNi$_x$(Pt$_{73}$Ni$_{27}$)/C], and 1.3 nm in wire diameter (9: Pt NW/C). Blue bars, yellow bars, and green bars depict 2.5−2.8 nm nanoparticles, 4.5 nm nanoparticles, and structured nanoparticles. RDE: room temp.; MEA: 353 K.
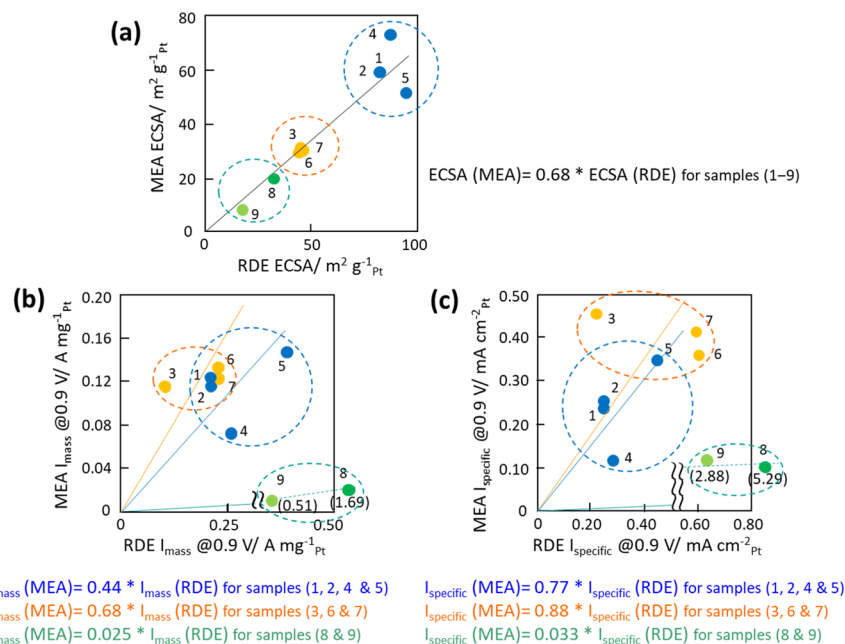

I_{mass} (MEA)= 0.44 * I_{mass} (RDE) for samples (1, 2, 4 & 5)
I_{mass} (MEA)= 0.68 * I_{mass} (RDE) for samples (3, 6 & 7)
I_{mass} (MEA)= 0.025 * I_{mass} (RDE) for samples (8 & 9)

$I_{specific}$ (MEA)= 0.77 * $I_{specific}$ (RDE) for samples (1, 2, 4 & 5)
$I_{specific}$ (MEA)= 0.88 * $I_{specific}$ (RDE) for samples (3, 6 & 7)
$I_{specific}$ (MEA)= 0.033 * $I_{specific}$ (RDE) for samples (8 & 9)

Figure 3. Relations between the RDE ECSA and MEA ECSA (a) and the RDE kinetic activities and MEA kinetic activities at 0.9 V (b and c). (b,c) ORR mass and specific activities at RDE and in MEA. 1 and 2: Pt/C (TEC10E50E), 3: Pt/C (TEC10E50E-HT), 4: Pt/C (TEC10E30E), 5: Pt/C (TEC10E30NC), 6: Pt$_3$Ni/C (TECNi52), 7: Pt$_3$Co/C (TEC36E52), 8: concave octahedral PtNi$_x$/C, and 9: Pt NW/C. (b) The values in parentheses for 8 and 9 are RDE I_{mass} at 0.9 V. (c) The values in parentheses for 8 and 9 are RDE $I_{specific}$ at 0.9 V. Voltage: vs RHE; RDE: room temp.; and MEA: 353 K. The linear relationship equations for the samples (1−9) are also shown.

have spectroscopically determined the kinetic reactivity and property of available surface Pt sites of the cathode electrocatalysts in MEA by measuring the structural kinetics of changes in Pt valence, coordination number of Pt−O bonds (CN$_{Pt−O}$), and coordination number of Pt−Pt bonds (CN$_{Pt−Pt}$) under transient voltage operations using the operando time-resolved Pt L$_{III}$-edge QXAFS technique.

Structural Kinetics and Reaction Rate Constants to Bring About the Cathode Nanoparticle Electrocatalysis

in MEA under Transient Voltage Operations. The ORR performance of Pt-based cathode electrocatalysts in MEA of PEFC as well as at RDE is relevant to the kinetics of the changes in both the electronic states (Pt-oxidation states) and bonding states (coordination numbers and interatomic distances of Pt−O and Pt−Pt bonds) of the nanoparticle electrocatalysts under PEFC operating conditions. However, under steady-state conditions, the electronic and bonding states of the cathode electrocatalysts remain almost unchanged, making it difficult to
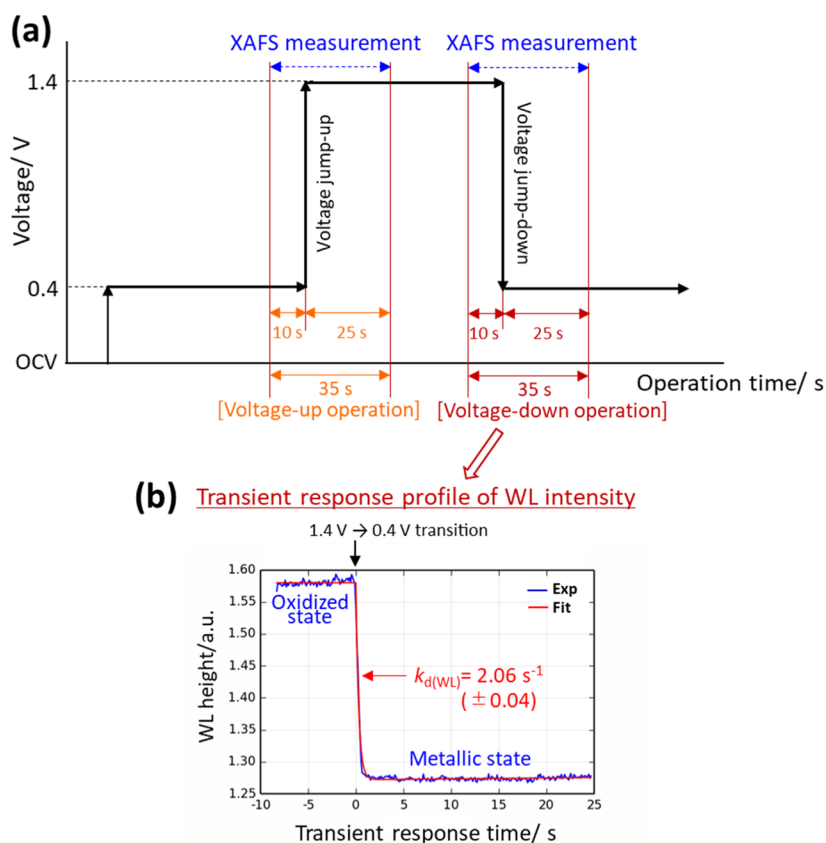
Figure 4. (a) Transient voltage-jump operation ($0.4 \rightarrow 1.4$ V) and voltage-down operation ($1.4 \rightarrow 0.4$ V) at the MEA cathode in PEFC and the period of QXAFS measurements at Pt L_{III}-edge in the transient response processes. Voltage: vs RHE. (b) Transient response profile of the white line (WL) intensity for standard Pt/C (TEC10E50E) under the transient voltage operation $1.4 \rightarrow 0.4$ V [H$_2$ (anode)-N$_2$ (cathode); cell temp.: 353 K, relative humidity: $\sim 93\%$], and the rate constant, $k_{d(WL)} = 2.06$ s^{-1} (± 0.04), determined by curve fitting (red curve) using an exponential function (eq 1 in the text).

observe dynamic changes in the electronic and structural states of active Pt sites at the cathode involved in the ORR processes. The structural kinetics (reaction kinetics based on the electronic and structural changes of electrocatalysts observed spectroscopically at the atomic level) of the cathode can be determined by time-resolved Pt L_{III}-edge QXAFS measurements during voltage transient response processes under H$_2$ (anode)−N$_2$ (cathode) conditions.[26,27,31,32,34] In the transient voltage operation, the cell voltage was changed from the open-circuit voltage to 0.4 V (vs RHE), held for 60 s, followed by a rapid voltage jump from 0.4 to 1.4 V, maintained for 60 s, and then quickly reduced from 1.4 to 0.4 V, as shown in Figure 4a. The transient responses of the MEA cathode electrocatalysts to the voltage cycling operations for 35 s from 10 s before each voltage jump were monitored by time-resolved QXAFS. The series of typical operando time-resolved Pt L_{III}-edge QXANES spectra (every 100 ms) and QEXAFS Fourier transforms (every 300 ms; 100 ms x 3 merged) for a standard Pt/C (TEC10E50E) under the transient voltage cyclic operations of $0.4 \rightarrow 1.4$ and $1.4 \rightarrow 0.4$ V are shown in Figure S6a,b.

As mentioned in the Introduction section, there is a linear relationship between the ORR performances of the MEA Pt-based electrocatalysts and the rate constants for the transformations of the Pt L_{III}-edge white line (WL) peak intensity and Pt−O coordination number (CN$_{Pt-O}$) in the MEA Pt-based electrocatalysts. There is also a linear relationship between the MEA Pt-based cathode durability and the inverse of the rate constant for the transformation of the Pt−Pt coordination

number (CN$_{Pt-Pt}$) (Figure S3).[30−32] The transient response profile of the WL intensity in the $1.4 \rightarrow 0.4$ V operation for standard MEA Pt/C (TEC10E50E) at 353 K is shown in Figure 4b. The rate constant $k_{d(WL)}$ for the change of the WL intensity under transient voltage operation was determined to be 2.06 s^{-1} (± 0.04) by data fitting (red curve) using an exponential function (eq 1).

$$\begin{aligned} f_{d\alpha}(t) &= y_{0\alpha} & t < 0 \\ &= y_{1\alpha} + a_{1\alpha}\exp(-k_{d(\alpha)}t) & t \geq 0 \\ a_{1\alpha} &= y_{0\alpha} - y_{1\alpha} \end{aligned} \tag{1}$$

The $k_{d(\alpha)}$ in eq 1 represents the rate constants for the changes in α under the transient voltage operation $1.4 \rightarrow 0.4$ V (α: WL, CN$_{Pt-O}$, or CN$_{Pt-Pt}$). The CN$_{Pt-O}$ and CN$_{Pt-Pt}$ were obtained by QEXAFS analysis, as typically shown in Figure S7A,B, which exhibits the curve-fitting results on k^2-weighted Pt L_{III}-edge QEXAFS oscillations and their associated Fourier transforms for MEA Pt/C (TEC10E50E) at 1.4 and 0.4 V. The structure models at 1.4 V (oxidized state) and 0.4 V (metallic state) in Figure S7C were estimated by the CN$_{Pt-O}$ and CN$_{Pt-Pt}$ and averaged particle size similar to previous reports.[29,31,34] The details of the time-resolved QXAFS measurements at the Pt L_{III}-edge and data analysis are described in the Supporting Information.

The transient response profiles for the WL intensity (peak height) of the Pt L_{III}-edge QXANES and the CN$_{Pt-O}$ obtained
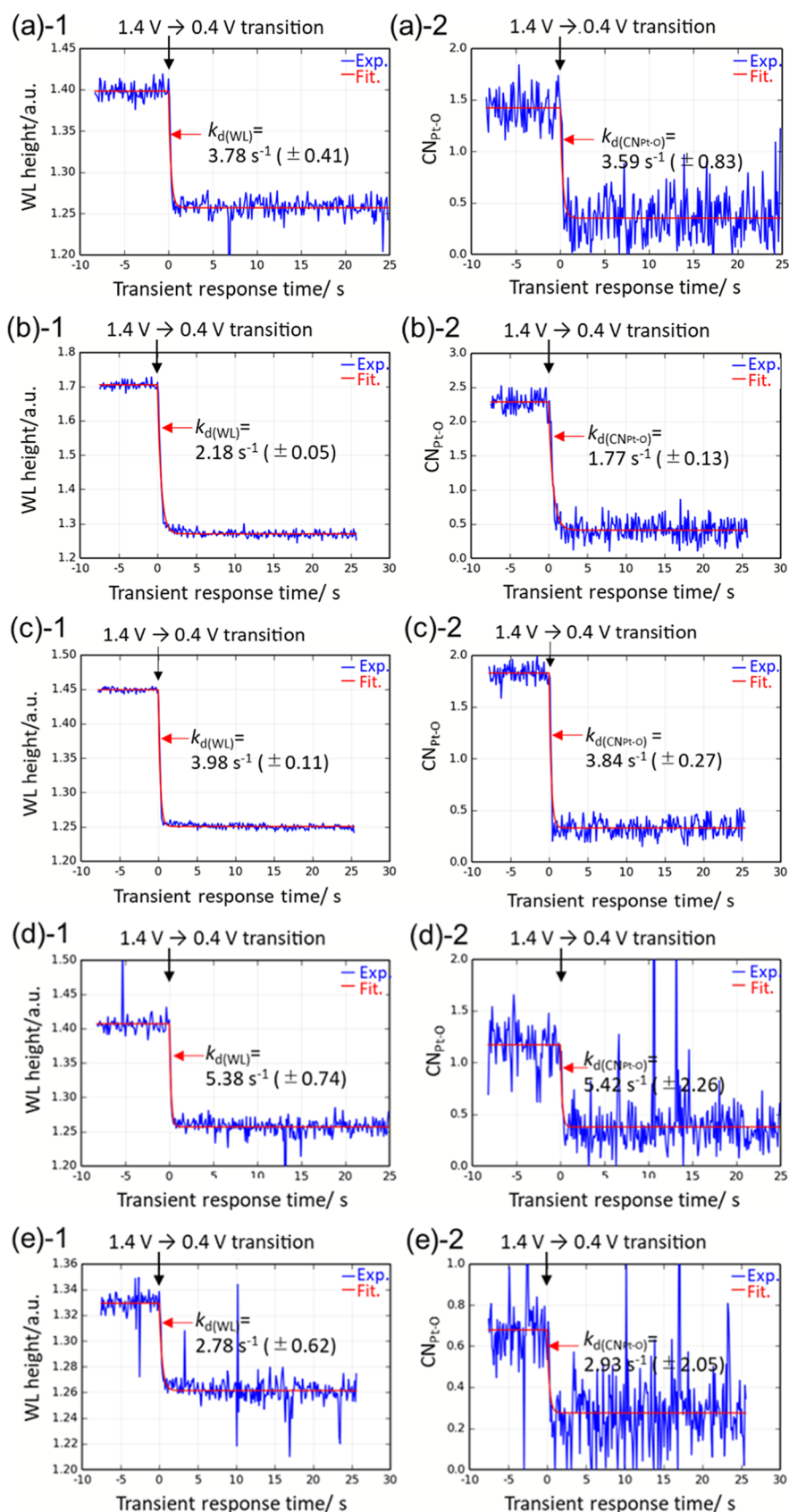
Figure 5. Transient response profiles of the WL intensity (a-1−e-1) and coordination number of Pt−O bond (CN_{Pt-O}) (a-2−e-2) in the transient voltage-down process (1.4 → 0.4 V vs RHE) for the following typical MEA cathodes; (a) Pt/C (TEC10E50E-HT), (b) Pt/C (TEC10E30E), (c) Pt_3Ni/C (TECNi52), (d) concave octahedral $PtNi_x$/C, and (e) Pt NW/C. The transient response profiles (blue) were fitted by one exponential function (red); $f_{d\alpha}(t) = y_{0\alpha}$ when $t < 0$ and $f_{d\alpha}(t) = y_{1\alpha} + a_{1\alpha} \exp(-k_{d(\alpha)} t)$ when $t \geq 0$, where $a_{1\alpha} = y_{0\alpha} - y_{1\alpha}$ $k_{d(\alpha)}$: rate constants, and α: WL or CN_{Pt-O}. H_2 (anode)−N_2 (cathode); cell temp.: 353 K; relative humidity: ~93%. XAFS acquisition: every 100 ms.
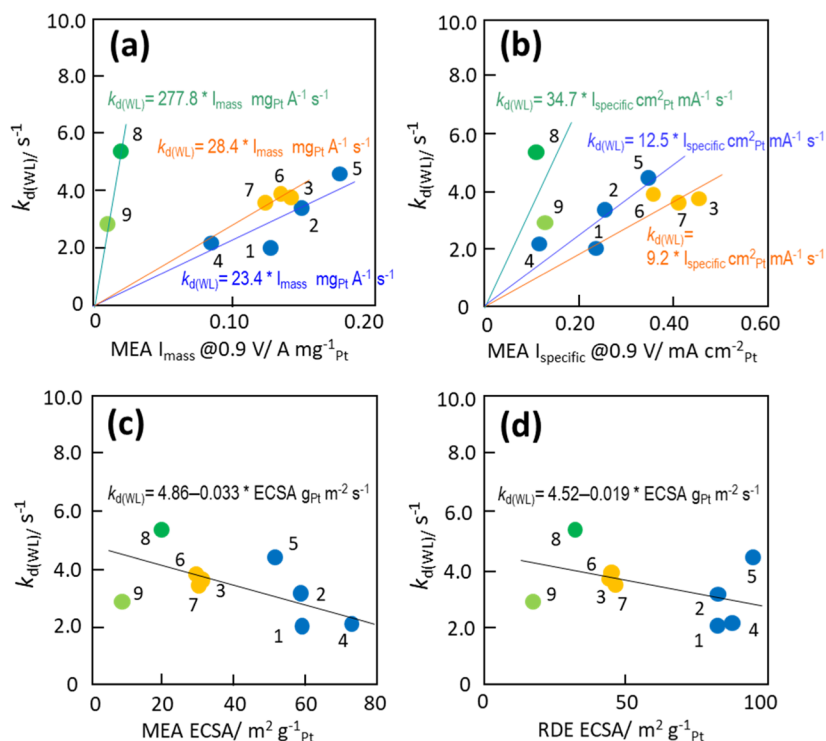
Figure 6. Relations between $k_{d(WL)}$ and MEA I_{mass} at 0.9 V (a), MEA $I_{specific}$ at 0.9 V (b), MEA ECSA (c), or RDE ECSA (d). $k_{d(WL)}$ is the rate constant of the transient response of WL height for the MEA samples under the voltage jump-down (1.4 V → 0.4 V) process. Voltage: vs RHE. 1 and 2: Pt/C (TEC10E50E), 3: Pt/C (TEC10E50E-HT), 4: Pt/C (TEC10E30E), 5: Pt/C (TEC10E30NC), 6: Pt$_3$Ni/C (TECNi52), 7: Pt$_3$Co/C (TEC36E52), 8: concave octahedral PtNi$_x$/C, and 9: Pt NW/C.
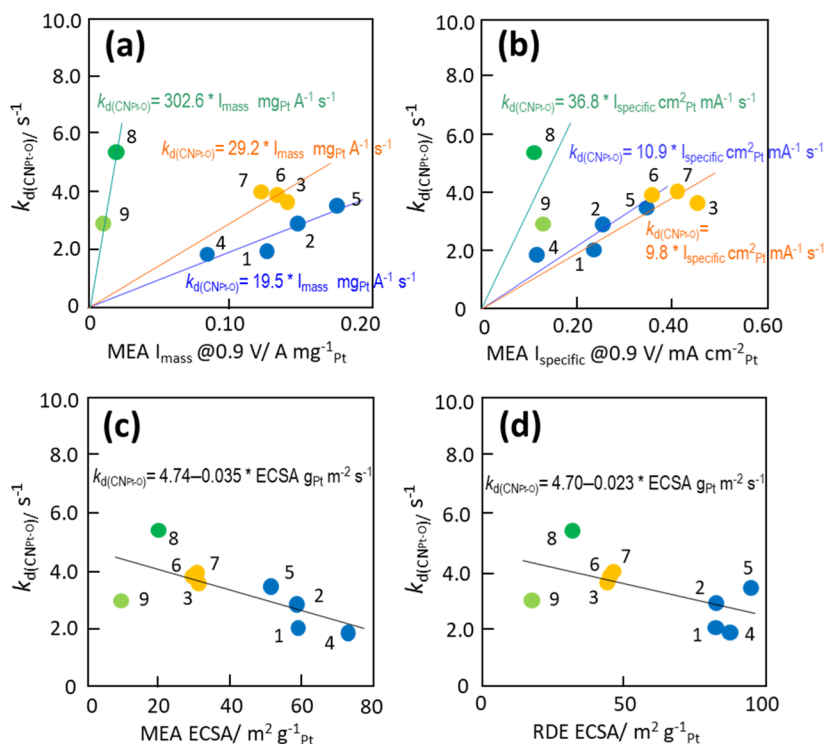

Figure 7. Relations between $k_{d(CN_{Pt-O})}$ and MEA I_{mass} at 0.9 V (a), MEA $I_{specific}$ at 0.9 V (b), RDE ECSA (c), or MEA ECSA (d). The $k_{d(CN_{Pt-O})}$ is the rate constant of the transient response of CN$_{Pt-O}$ for the MEA samples under the voltage-down (1.4 → 0.4 V) process. Voltage: vs RHE. 1 and 2: Pt/C (TEC10E50E), 3: Pt/C (TEC10E50E-HT), 4: Pt/C (TEC10E30E), 5: Pt/C (TEC10E30NC), 6: Pt$_3$Ni/C (TECNi52), 7: Pt$_3$Co/C (TEC36E52), 8: concave octahedral PtNi$_x$/C, and 9: Pt NW/C.

by QEXAFS analysis for other typical MEA cathode samples examined in this study were plotted against the transient response time (t) under the voltage operation 1.4→ 0.4 V in Figure 5; a-1 and a-2: Pt/C (TEC10E50E-HT), b-1 and b-2: Pt/

C (TEC10E30E), c-1 and c-2: Pt$_3$Ni/C (TECNi52), d-1 and d-2: concave octahedral PtNi$_x$ (Pt$_{73}$Ni$_{27}$)/C (fabricated by us); and e-1 and e-2: Pt NW/C (fabricated by us). The rate constants for these transient response profiles were estimated by the exponential function (eq 1), as shown by the red curves in Figure 5 as follows: $k_{d(WL)}$ = 3.78 ($\pm$0.41) s^{-1}, 2.18 ($\pm$0.05) s^{-1}, 3.98 ($\pm$0.11) s^{-1}, 5.38 ($\pm$0.74) s^{-1}, and 2.78 ($\pm$0.62) s^{-1}, respectively, and $k_{d(CN_{Pt-O})}$ = 3.59 ($\pm$0.83) s^{-1}, 1.77 ($\pm$0.13) s^{-1}, 3.84 ($\pm$0.27) s^{-1}, 5.42 ($\pm$2.26) s^{-1}, and 2.93 ($\pm$2.05) s^{-1}, respectively. Rapid changes in the WL peak height and CN$_{Pt-O}$ and CN$_{Pt-Pt}$ were observed when the cell voltage was changed under H$_2$ (anode)$-$N$_2$ (cathode). It has been demonstrated that the transient response changes in the electrocatalysts under H$_2$ (anode)$-$air (cathode) are smaller than those under H$_2$ (anode)$-$N$_2$ (cathode) due to remaining partially oxidized cathode Pt surfaces at 0.4 V under air (cathode), but the trend and structural kinetics of the changes in the WL peak height, CN$_{Pt-O}$, and CN$_{Pt-Pt}$ are essentially similar under the both conditions.[32] It should be noted that the first-order rate constants determined by the exponential function analysis are independent of Pt density and Pt utilization in MEA. Hence, the first-order rate constants directly reflect the kinetic reactivity and properties of available active Pt sites at the cathode electrocatalyst surfaces in MEA.

Correlations between the Structural Kinetics [$k_{d(WL)}$, $k_{d(CN_{Pt-O})}$, and $k_{d(CN_{Pt-Pt})}$] and Electrochemical Property (I_{mass}, $I_{specific}$, and ECSA) for MEA Samples: Similarity and Difference. As described in the Introduction section, the rate constants for the transformations of the WL intensity and CN$_{Pt-O}$ in MEA Pt-based electrocatalysts under the transient voltage operations show linear relationships with the ORR performances of the MEA cathodes.[30,31] Figures 6 and 7 illustrate the correlations between $k_{d(WL)}$ or $k_{d(CN_{Pt-O})}$ and I_{mass} (MEA) at 0.9 V (a), $I_{specific}$ (MEA) at 0.9 V (b), ECSA (MEA) (c), or ECSA (RDE) (d) for samples 1 through 9. The $k_{d(WL)}$ and $k_{d(CN_{Pt-O})}$ are the first-order rate constants determined by eq 1 for the changes in the WL height and CN$_{Pt-O}$, respectively, in the MEA cathode electrocatalysts (1−9) under transient voltage operations (1.4 → 0.4 V vs RHE), as shown in Figure 5. It was found that the correlations between the rate constants ($k_{d(WL)}$ and $k_{d(CN_{Pt-O})}$) and electrochemical activities (MEA I_{mass} and MEA $I_{specific}$) in Figures 6 and 7 fall into three distinct linear categories with different slopes (blue, yellow, and green). The calculated correlation equations are presented in Figures 6a,b and 7a,b. Conversely, the plots of $k_{d(WL)}$ vs ECSA (MEA) in Figure 6c and $k_{d(CN_{Pt-O})}$ vs ECSA (MEA) in Figure 7c for all samples (1−9) lie on the same straight lines with negative slopes, as shown by the calculated correlation equations in Figures 6c and 7c, respectively. The smaller the ECSAs (MEA), the larger the rate constants became in the ECSA range of 8−75 m^2 g^{-1}$_{Pt}$. Similar trends were also observed for ECSA (RDE) in the range of 17−95 m^2 g^{-1}$_{Pt}$ (Figures 6d and 7d). These results present a dilemma in the context of an increasing mass activity.

The correlation coefficients for $k_{d(WL)}$ vs $I_{specific}$ (MEA) and $k_{d(CN_{Pt-O})}$ vs $I_{specific}$ (MEA) in Figures 6b and 7b were estimated as follows: 12.5 and 10.9 (11.7 on average) for samples 1, 2, 4, and 5; 9.2 and 9.8 (9.5 on average) for samples (3, 6, and 7); and 34.7 and 36.8 (35.8 on average) for samples (8 and 9), respectively. The correlation equations for $k_{d(WL)}$ vs $I_{specific}$ (MEA) and $k_{d(CN_{Pt-O})}$ vs $I_{specific}$ (MEA) in Figures 6b and 7b, respectively,

coincide with those calculated from I_{mass}/ECSA (Figures 6a and 7)a, which may justify that the rate constants $k_{d(WL)}$ and $k_{d(CN_{Pt-O})}$ are categorized along three different lines (blue, yellow, and green). The kinetic activities of available Pt sites at the surface of the cathode electrocatalysts in MEAs are characterized by the first-order rate constants $k_{d(WL)}$ and $k_{d(CN_{Pt-O})}$.[30,31] The rate constants (intrinsic surface specific activity) of MEA samples (8 and 9) on average were found to be 3.1 and 3.8 times larger than those for samples (1, 2, 4, and 5) and samples (3, 6, and 7) on average, respectively. However, the electrochemically determined $I_{specific}$ (MEA) values for samples (8 and 9) in Figures 2, 3, 6, and 7 were so small as 0.099 and 0.118 mA cm^{-2}$_{Pt}$, respectively (0.11 mA cm^{-2}$_{Pt}$ on average), which is only 1/4.2 and 1/3.4, respectively (approximately one-fourth) of the average $I_{specific}$ (MEA) (0.41 mA cm^{-2}$_{Pt}$) for three samples (3, 6, and 7) as typical examples.

Namely, the intrinsic kinetic activities of available Pt sites at the cathode electrocatalyst surfaces in MEA samples (8 and 9), determined spectroscopically by the operando time-resolved QXAFS at the Pt L$_{III}$-edge, were evaluated to be 15.7 and 13.2 times larger, respectively, than the $I_{specific}$ (MEA) estimated electrochemically. Thus, it was found that MEA samples (8 and 9) inherently possess the high $I_{specific}$ (MEA) capabilities of 1.55 mA cm^{-2}$_{Pt}$ and 1.56 mA cm^{-2}$_{Pt}$, respectively, as shown as graduated blue bars (d) in Figure 8. Notably, the RDE−MEA gap (RDE:MEA ratio) in the $I_{specific}$ activity reduced remarkably from 53.8:1 to 3.5:1 and from 24.6:1 to 1.86:1 for the samples (8
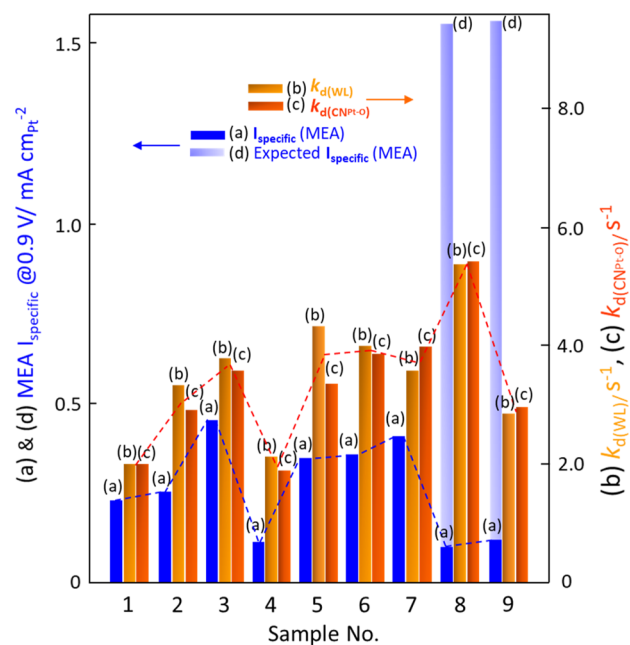

Figure 8. ORR kinetic activities (surface specific activities) at 0.90 V for samples 1−9 in MEA (a) and rate constants, $k_{d(WL)}$ (b) and $k_{d(CN_{Pt-O})}$ (c), of the transient response of WL and CN$_{Pt-O}$, respectively, for the MEA samples under the voltage-down (1.4 → 0.4 V) process. Voltage: vs RHE. (d) $I_{specific}$ (MEA) values (1.55 mA cm$_{Pt}^{-2}$ and 1.56 mA cm$_{Pt}^{-2}$) expected from the $k_{d(WL)}$ and $k_{d(CN_{Pt-O})}$ for the MEA samples (8 and 9), respectively (see the text). Cathode electrocatalyst samples: (1 and 2) Pt/C (TEC10E50E), (3) Pt/C (TEC10E50E-HT), (4) Pt/C (TEC10E30E), (5) Pt/C (TEC10E30NC), (6) Pt$_3$Ni/C (TECNi52), (7) Pt$_3$Co/C (TEC36E52), (8) concave octahedral PtNi$_x$/C, and (9) Pt NW/C.

and 9), respectively. As a result, the $I_{specific}$ (MEA) activities expected from the transient kinetics for the samples (8 and 9) are 3.1–3.8 times higher than those of the other samples (1–7), even though the electrochemically measured $I_{specific}$ (MEA) values for the samples (8 and 9) were 3.4–4.2 times lower than those for the samples (1–7). The electrochemically decided $I_{specific}$ (MEA) and transient spectroscopically decided $k_{d(WL)}$ and $k_{d(CN_{Pt-O})}$ for MEA samples (1–9) are shown in Figure 8 for comparison. In contrast to the large performance loss in MEA against the remarkable performance $I_{specific}$ at RDE for the structured electrocatalysts (8 and 9) in Figure 2, the $k_{d(WL)}$ and $k_{d(CN_{Pt-O})}$, corresponding to inherent kinetic activities, for the MEA samples (8 and 9) are larger than the average $k_{d(WL)}$ and $k_{d(CN_{Pt-O})}$ of the other spherical electrocatalysts (1–7) in MEA (Figure 8). The changes in the $k_{d(WL)}$ and $k_{d(CN_{Pt-O})}$ nearly trace the changes in the $I_{specific}$ for the MEA samples (1–7), but the trend of the changes in the $k_{d(WL)}$ and $k_{d(CN_{Pt-O})}$ for the MEA samples (8 and 9) is entirely different from that of the changes in the $I_{specific}$. The transient response profiles determined by the transient QXAFS analysis reveal the kinetically good levels of MEA performance (Figure 8) despite the large RDE–MEA gaps in the electrochemically determined I_{mass} and $I_{specific}$ (Figures 6 and 7).

Nevertheless, the spectroscopically expected $I_{specific}$ (MEA) values for samples (8 and 9) did not reproduce their remarkable $I_{specific}$ (RDE) values completely as one can see from the comparison of the $I_{specific}$ (RDE) and $I_{specific}$ (MEA)/expected $I_{specific}$ (MEA) values for the samples (1–9) in Figures 3 and 8. The reason may be attributed to the coexistence of less active Pt sites in addition to the highly active Pt sites,[33] leading to the lower average $I_{specific}$ (MEA) values than the case of the presence of only the highly active Pt sites because the QXAFS analysis provides averaged information on all electrocatalyst nanoparticles present in the samples. In the case of the presence of only the highly active Pt sites (no contribution of the other Pt sites to the $k_{d(WL)}$ and $k_{d(CN_{Pt-O})}$) in MEA, only 6.4–7.6% (1/15.7–1/13.2) of the available Pt sites at the cathode electrocatalyst surfaces in MEA samples (8 and 9) are regarded to work as active sites for ORR performances from the comparison of the inherent kinetic activities of available Pt sites determined spectroscopically with the $I_{specific}$ estimated electrochemically as above-discussed. Increasing utilization of ineffective Pt sites at the electrocatalyst surfaces in the cathode layer may need interface engineering in MEA. However, the current MEA manufacturing process does not maximize Pt utilization,[41–43] necessitating the development of intelligent interface engineering on carbon assemblies to enhance the ORR performance.[21]

Further, so-called layer effects on overall PEFC performances may be significant, and proper design and optimization of the PEFC layers are essential for maximizing power output, efficiency, and durability of PEFC. Electrochemical impedance spectroscopy (EIS) provides a valuable insight into the dynamic behavior and interaction of cathode catalyst layer, proton exchange membrane, and gas diffusion layer under PEFC operating conditions.[44,45] However, the aim of our study is to correlate the ORR catalytic performance of the cathode layer selectively and directly with the kinetic reactivity and structural kinetics of available surface Pt sites at the cathode (catalyst activity itself), eliminating other parameters, which is hard to do by EIS.

Previously, we found that the relaxation time (the reciprocal of rate constants) of Pt–Pt bond reformation in MEA Pt/C cathodes under transient voltage operations (1.4 → 0.4 V) predicts the relative durability of the cathode electrocatalysts in MEAs without long-term experimental durability tests.[26,27,30,31] Transient response profiles of CN_{Pt-Pt} in the voltage operation process (1.4 → 0.4 V) for Pt_3Ni/C (TECNi52) and Pt_3Co/C (TEC36E52) as typical examples of MEA cathodes are shown in Figure S8. The transient response curves (blue) were fitted by one exponential function (red) (eq 1), yielding rate constants $k_{d(CN_{Pt-Pt})}$ of 3.26 s^{-1} ($\pm$0.46) and 3.42 s^{-1} ($\pm$0.58) for Pt_3Ni/C (TECNi52) and Pt_3Co/C (TEC36E52), respectively. Figure 9
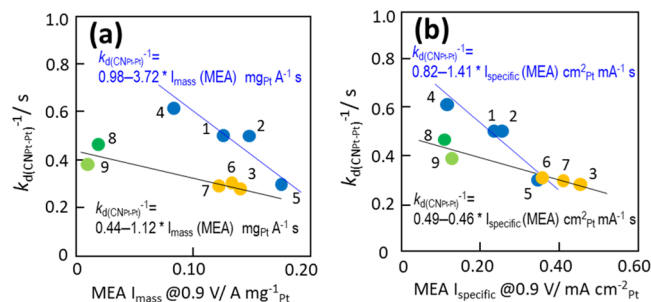

Figure 9. Relations between $k_{d(CN_{Pt-Pt})}^{-1}$ (relaxation time) and MEA I_{mass} at 0.9 V (a) or MEA $I_{specific}$ at 0.9 V (b). The $k_{d(CN_{Pt-Pt})}^{-1}$ is the reciprocal of the rate constant of the transient response of CN_{Pt-Pt} for the MEA samples under the voltage jump-down (1.4 → 0.4 V) process. Voltage: vs RHE. 1 and 2: Pt/C (TEC10E50E), 3: Pt/C (TEC10E50E-HT), 4: Pt/C (TEC10E30E), 5: Pt/C (TEC10E30NC), 6: Pt_3Ni/C (TECNi52), 7: Pt_3Co/C (TEC36E52), 8: concave octahedral $PtNi_x/C$, and 9: Pt NW/C.

presents the relationships between the relaxation time $k_{d(CN_{Pt-Pt})}^{-1}$ and MEA I_{mass} at 0.9 V (a) or MEA $I_{specific}$ at 0.9 V (b) for all samples (1–9). The plots of $k_{d(CN_{Pt-Pt})}^{-1}$ vs I_{mass} (MEA) (a) and $k_{d(CN_{Pt-Pt})}^{-1}$ vs $I_{specific}$ (MEA) (b) for samples (1, 2, 4, and 5) and samples (3, 6, 7, 8, and 9) are correlated by the following equations with negative slopes, respectively: $k_{d(CN_{Pt-Pt})}^{-1}$ = 0.98–3.72 × I_{mass} (MEA) mg$_{Pt}$ A^{-1} s and $k_{d(CN_{Pt-Pt})}^{-1}$ = 0.82–1.41 × $I_{specific}$ (MEA) cm$^2_{Pt}$ mA^{-1} s for samples (1, 2, 4, and 5), and $k_{d(CN_{Pt-Pt})}^{-1}$ = 0.44–1.12 × I_{mass} (MEA) mg$_{Pt}$ A^{-1} s and $k_{d(CN_{Pt-Pt})}^{-1}$ = 0.49–0.46 × $I_{specific}$ (MEA) cm$^2_{Pt}$ mA^{-1} s for samples (3, 6, 7, 8, and 9). As the MEA I_{mass} and MEA $I_{specific}$ increase, the durability of the samples (1, 2, 4, and 5) with the larger coefficients in the correlation equations decreases more than that of the samples (3, 6, 7, 8, and 9) with the smaller coefficients. As a whole, the smaller the I_{mass} and $I_{specific}$, the larger the $k_{d(CN_{Pt-Pt})}^{-1}$ becomes. In other words, as the electrochemical ORR activity of MEA samples increases, the durability of the MEA samples decreases, showing a dilemma for development of new electrocatalysts for PEFC. The relaxation time $k_{d(CN_{Pt-Pt})}^{-1}$ was nearly independent of the ECSAs in MEA and at RDE, as shown in Figure S9a,b, though the data are a little scattered, indicating that ECSA is not a primary regulation factor for development of new next-generation PEFC electrocatalysts.

■ CONCLUSIONS

(1) To understand the ORR performance gap between RDE and MEA, we have spectroscopically determined the

transient response profiles and rate constants, $k_{d(WL)}$, $k_{d(CN_{Pt-O})}$, and $k_{d(CN_{Pt-Pt})}$, for changes in the WL intensity, CN_{Pt-O}, and CN_{Pt-Pt} of nine representative cathode electrocatalysts with different types and performances under transient voltage operations (1.4 → 0.4 V) using the operando element-selective time-resolved Pt L_{III}-edge QXAFS technique.

(2) For the first time, the transient kinetics and property of available surface Pt sites in the cathode layers of MEAs were systematically compared with the I_{mass} and $I_{specific}$ of the electrocatalysts in MEA and at RDE.

(3) The I_{mass} (MEA) and $I_{specific}$ (MEA) of electrocatalysts (1−7) with spheric shapes of 2.5−4.5 nm sizes correlated proportionally with the I_{mass} (RDE) and $I_{specific}$ (RDE), whereas the I_{mass} (MEA) and $I_{specific}$(MEA) of structured electrocatalysts [concave octahedral $PtNi_x$/C (8) and Pt NW/C (9)] did not correlate with the corresponding I_{mass} (RDE) and $I_{specific}$ (RDE).

(4) The first-order rate constants determined by transient QXAFS analysis are independent of Pt density and Pt utilization in MEA, providing direct information on the intrinsic kinetic reactivity and property of available surface Pt sites that contribute to MEA cathode electrocatalysis.

(5) The intrinsic kinetic activities ($k_{d(WL)}$ and $k_{d(CN_{Pt-O})}$) of available Pt sites in MEA samples (8 and 9) determined spectroscopically were evaluated to be 15.7 and 13.2 times larger than the $I_{specific}$ (MEA) estimated electrochemically, respectively. Consequently, the RDE−MEA gap (RDE:-MEA ratio) for samples (8 and 9) reduced remarkably from 53.8:1 to 3.5:1 and from 24.6:1 to 1.86:1, respectively.

(6) The spectroscopically expected $I_{specific}$ (MEA) activities for samples (8 and 9) were found to be 3.1−3.8 times higher than those of other samples (1−7) on overage, even though the electrochemically measured $I_{specific}$ (MEA) values for samples (8 and 9) were 3.4−4.2 times lower than those for the samples (1−7). The transient response profiles suggest good kinetic performances of MEAs despite large RDE−MEA gaps in electrochemically determined I_{mass} and $I_{specific}$.

(7) So-called layer effects on overall PEFC performances may be significant, and proper design and optimization of the PEFC layers are essential for maximizing power output, efficiency, and durability of PEFC.

(8) Assuming that other Pt sites than the highly active Pt sites among all Pt sites at the cathode layer make no contribution to $k_{d(WL)}$ and $k_{d(CN_{Pt-O})}$, it was estimated that only 6.4−7.6% of the available Pt sites at the cathode electrocatalyst surfaces act as active sites for ORR performances in MEA samples (8 and 9). Increasing utilization of ineffective Pt sites at the electrocatalyst surfaces in the cathode layer may need interface engineering in MEA.

(9) As the electrochemical ORR activities of MEA samples increased, their durability decreased. The relaxation time $k_{d(CN_{Pt-Pt})}^{-1}$ was nearly independent of the ECSAs in MEA and at RDE, indicating minimal impact of ECSAs on developing robust cathode electrocatalysts.

(10) Although MEA manufacturing for the highest Pt utilization has not yet been perfected, the operando kinetic findings under transient response operations provide new insights into understanding the cause of

the RDE−MEA gap and the development of next-generation PEFCs with high performance and durability.

■ EXPERIMENTAL SECTION

Carbon (Ketjen Black)-Supported Electrocatalysts. 50 wt %-Pt/C (TEC10E50E), 50 wt %-Pt/C (TEC10E50E-HT), 30 wt %-Pt/C (TEC10E30E), 30 wt %-Pt/C (TEC10E30NC), 45 wt %(5 wt %-Ni)-Pt_3Ni/C (TECNi52), and 45 wt %(5 wt %-Co)-Pt_3Co/C (TEC36E52) were purchased from Tanaka Kikinzoku Kogyo (TKK). Concave octahedral $Pt_{73}Ni_{27}$/C (denoted as $PtNi_x$/C, 19.1 wt %-Pt) was synthesized in a similar way to that described in our previous work.[7] The fabrications of regular polycrystalline Pt nanowires (Pt NW) and 20 wt %-Pt NW/C followed the previous method.[46,47] Detailed characterizations of the Pt and Pt-alloy nanoparticles by TEM and XRF are provided in the Supporting Information.

Electrochemical Measurements at RDE. Detailed electrochemical experiments including CV, LSV (anodic polarization), ORR, and ECSA measurements are described in the Supporting Information. The electrochemical properties of the catalysts at RDE were assessed in 0.1 M $HClO_4$ typically by using 10 μL of a mixture of absolute ethanol (1.75 mL) (0.4 mL of isopropanol in the case of $PtNi_x$/C and Pt NW/C),[6,7,46] ultrapure (18.2 MΩ·cm Millipore) water (750 μL), 5% Nafion solution (25 μL), and catalyst powder (4.4 μg-Pt cm^{-2}). This mixture was deposited on a glassy carbon electrode (ϕ = 5 mm) and dried at room temperature under ambient conditions. Solution resistance was measured by the i-interrupter method for IR compensation.[6]

Electrochemical Measurements of MEA in PEFC. MEAs with an electrode area of 3.0 × 3.0 cm^2 were purchased from the EIWA Corporation. The Pt densities at the cathode in MEAs were 0.61−0.63 mg-Pt cm^{-2}. Ru/C (TECRu(ONLY)E50, TKK) was used as the anode catalyst to avoid interference with XAFS signals of the cathode catalysts from the anode catalyst. The MEAs were mounted into custom-built in situ XAFS fuel cells using Viton gaskets with 0.15 mm thickness, gas diffusion layers (GDL; TGP-H-060, TORAY), and separator plates with serpentine-shaped gas flow channels for both anode and cathode sides.[29,35] The cathode was connected as a working electrode in the PEFC XAFS cell, while the anode (hydrogen-fed) served as the combined counter and reference electrode. All potentials in MEA experiments were referred to this pseudo hydrogen reference electrode (RHE). Cyclic voltammetry was performed between 0.05 and 0.9 V at a sweep rate of 20 mV s^{-1} in H_2 (anode) and N_2 (cathode) to estimate ECSAs of the cathode catalysts in the MEAs at 353 K. Mass activities and surface specific activities of the MEA cathodes were calculated from the kinetic activities at 0.9 V, which were evaluated by semilogarithmic plots of I−V polarization curves in H_2 (anode) and air (cathode).[38] A typical example is shown in Figure 1 (f) (inset) and Figure S4. Additional experimental details are provided in the Supporting Information.

Operando Time-Resolved QXAFS Measurements, Data Analysis, and Structural Kinetics. The details of time-resolved QXAFS measurements and data analysis are described in the Supporting Information, which are briefly summarized below. The series of operando time-resolved QXAFS spectra at Pt L_{III}-edge for the cathode electrocatalysts in the MEAs under transient voltage operations (1.4 → 0.4 V vs RHE) were measured in a transmission mode at BL36XU in SPring-8 (Figure S2).[31] QXAFS spectra were analyzed using the

Larch code containing the IFEFFIT Package ver.2 (Athena and Artemis)[26,48,49] in a similar way to the previous reports.[29,31,32,35] The phase shifts and amplitude functions for Pt−Pt and Pt−O were computed using the FEFF 8.4 code, based on structural parameters obtained from the crystal structures of Pt foil, PtO, and PtO_2.[26,50]

■ ASSOCIATED CONTENT

ⓈⒾ Supporting Information

The Supporting Information is available free of charge at https://pubs.acs.org/doi/10.1021/acsomega.4c07787.

> Experimental details; operando time-resolved QXAFS measurements and data analysis; Tafel plot for the concave octahedral $PtNi_x$/C in MEA as a typical electrochemical analysis example; operando time-resolved QXAFS measurement system; k^2-weighted Pt L_{III}-edge QEXAFS data and curve fitting results for Pt/C (TEC10E50E) at 0.4 and 1.4 V; relations between I_{mass} and $I_{specific}$ at RDE and in MEA for the samples (1−9); and transient response profiles of $CN_{Pt−Pt}$ under the transient voltage operation for Pt_3Ni/C (TECNi52) and Pt_3Co/C (TEC36E52) (PDF)

■ AUTHOR INFORMATION

Corresponding Author

Yasuhiro Iwasawa − *Innovation Research Center for Fuel Cells and Hydrogen, The University of Electro-Communications, Tokyo 182-8585, Japan; RIKEN SPring-8 Center, Physical and Chemical Research Infrastructure Group, Sayo, Hyogo 679-5148, Japan; Department of Engineering Science, Graduate School of Informatics and Engineering, The University of Electro-Communications, Tokyo 182-8585, Japan;* ⓞ orcid.org/0000-0002-5222-5418; Phone: +81-42-443-5921; Email: iwasawa@pc.uec.ac.jp

Authors

Takefumi Yoshida − *Innovation Research Center for Fuel Cells and Hydrogen, The University of Electro-Communications, Tokyo 182-8585, Japan; RIKEN SPring-8 Center, Physical and Chemical Research Infrastructure Group, Sayo, Hyogo 679-5148, Japan;* Present Address: Cluster of Nanomaterials, Graduate School of Systems Engineering, Wakayama University, Sakae-Dani, Wakayama 640-8510, Japan; ⓞ orcid.org/0000-0003-3479-7890

Shinobu Takao − *Innovation Research Center for Fuel Cells and Hydrogen, The University of Electro-Communications, Tokyo 182-8585, Japan*

Hiroko Ariga-Miwa − *Innovation Research Center for Fuel Cells and Hydrogen, The University of Electro-Communications, Tokyo 182-8585, Japan; RIKEN SPring-8 Center, Physical and Chemical Research Infrastructure Group, Sayo, Hyogo 679-5148, Japan*

Xiao Zhao − *Innovation Research Center for Fuel Cells and Hydrogen, The University of Electro-Communications, Tokyo 182-8585, Japan;* Present Address: Key Laboratory of Automobile Materials of MOE, School of Materials Science and Engineering, Jilin University, Changchun 130012, China.

Gabor Samjeské − *Department of Chemistry, Graduate School of Science, Nagoya University, Nagoya, Aichi 464-8602, Japan*

Takuma Kaneko − *Innovation Research Center for Fuel Cells and Hydrogen, The University of Electro-Communications, Tokyo 182-8585, Japan; Japan Synchrotron Radiation Research Institute, Hyogo 679-5198, Japan*

Tomoya Uruga − *Innovation Research Center for Fuel Cells and Hydrogen, The University of Electro-Communications, Tokyo 182-8585, Japan; Japan Synchrotron Radiation Research Institute, Hyogo 679-5198, Japan*

Complete contact information is available at:
https://pubs.acs.org/10.1021/acsomega.4c07787

Author Contributions

[∇]T.Y., S.T., and H.A-M. contributed equally. The manuscript was written through contributions of all authors. All authors have given approval to the final version of the manuscript.

Notes

The authors declare no competing financial interest.

■ ACKNOWLEDGMENTS

■ REFERENCES

(1) IEA. *Energy Consumption in Road Transport in Selected IEA Countries, 2000−2018 (IEA, 7 December 2020)*; Nature Electronics, 2022.

(2) Debe, K. Electrocatalyst Approaches and Challenges for Automotive Fuel Cells. *Nature* **2012**, *486*, 43−51.

(3) Zhang, L.; Roling, L. T.; Wang, X.; Vara, M. V.; Chi, M.; Liu, J.; Choi, S.; Park, J.; Herron, J. A.; Xie, Z.; Mavrikakis, M.; Xia, Y. Platinum-Based Nanocages with Subnanometer-Thick Walls and Well-Defined, Controllable Facets. *Science* **2015**, *349*, 412−416.

(4) Escudero-Escribano, M.; Malacrida, P.; Hansen, M. H.; Vej-Hansen, U. G.; Velázquez-Palenzuela, A.; Tripkovic, V.; Schiøtz, J.; Rossmeisl, J.; Stephens, I. E. L.; Chorkendorff, I. Tuning the Activity of Pt Alloy Electrocatalysts by Means of the Lanthanide Contraction. *Science* **2016**, *352*, 73−76.

(5) Mistry, H.; Varela, A. S.; Kühl, S.; Strasser, P.; Cuenya, B. R. Nanostructured Electrocatalysts with Tunable Activity and Selectivity. *Nature Rev. Mater.* **2016**, *1*, 16009.

(6) Nagasawa, K.; Takao, S.; Nagamatsu, S.; Samjeské, G.; Sekizawa, O.; Kaneko, T.; Higashi, K.; Yamamoto, T.; Uruga, T.; Iwasawa, Y. Surface-Regulated Nano-SnO_2/Pt_3Co/C Cathode Catalysts for Polymer Electrolyte Fuel Cells Fabricated by a Selective Electrochemical Sn Deposition Method. *J. Am. Chem. Soc.* **2015**, *137*, 12856−12864.

(7) Zhao, X.; Takao, S.; Higashi, K.; Kaneko, T.; Samjeskè, G.; Sekizawa, O.; Sakata, T.; Yoshida, Y.; Uruga, T.; Iwasawa, Y. Simultaneous Improvements in Performance and Durability of an Octahedral $PtNi_x$/C Electrocatalyst for Next-Generation Fuel Cells by Continuous, Compressive, and Concave Pt Skin Layers. *ACS Catal.* **2017**, *7*, 4642−4654.

(8) Chen, C.; Kang, Y.; Huo, Z.; Zhu, Z.; Huang, W.; Xin, H. L.; Snyder, J. D.; Li, D.; Herron, J. A.; Mavrikakis, M.; Chi, M.; More, K. L.; Li, Y.; Markovic, N. M.; Somorjai, G. A.; Yang, P.; Stamenkovic, V. R.; Stamenkovic, V. R. Highly Crystalline Multimetallic Nanoframes with Three-Dimensional Electrocatalytic Surfaces. *Science* **2014**, *343*, 1339−1343.

(9) Shao, M.; Chang, Q.; Dodelet, J.-P.; Chenitz, R. Recent Advances in Electrocatalysts for Oxygen Reduction Reaction. *Chem. Rev.* **2016**, *116*, 3594−3657.

(10) Li, M. F.; Zhao, Z. P.; Cheng, T.; Fortunelli, A.; Chen, C. Y.; Yu, R.; Zhang, Q. H.; Gu, L.; Merinov, B. V.; Lin, Z.; Zhu, E. B.; Yu, T.; Jia, Q. Y.; Guo, J. H.; Zhang, L.; Goddard, W. A.; Huang, Y.; Duan, X. F. Ultrafine Jagged Platinum Nanowires Enable Ultrahigh Mass Activity for the Oxygen Reduction Reaction. *Science* **2016**, *354*, 1414−1419.

(11) Seh, Z. W.; Kibsgaard, J.; Dickens, C. F.; Chorkendorff, I.; Nørskov, J. K.; Jaramillo, T. F. Combining Theory and Experiment in Electrocatalysis: Insights into Materials Design. *Science* **2017**, *355*, 6321.

(12) Liu, M. L.; Zhao, Z. P.; Duan, X. F.; Huang, Y. Nanoscale structure design for high performance Pt-based ORR catalysts. *Adv. Mater.* **2019**, *31*, No. e1802234.

(13) Stamenkovic, V. R.; Mun, B. S.; Arenz, M.; Mayrhofer, K. J. J.; Lucas, C. A.; Wang, G. F.; Ross, P. N.; Markovic, N. M. Trends in electrocatalysis on extended and nanoscale Pt-bimetallic alloy surfaces. *Nat. Mater.* **2007**, *6*, 241−247.

(14) Huang, J.; Sementa, L.; Liu, Z.; Barcaro, G.; Feng, M.; Liu, E.; Jiao, L.; Xu, M.; Leshchev, D.; Lee, S.-J.; Li, M.; Wan, C.; Zhu, E.; Liu, Y.; Peng, B.; Duan, X.; Goddard III, W. A.; Fortunelli, A.; Jia, Q.; Huang, Y. Experimental Sabatier plot for predictive design of active and stable Pt-alloy oxygen reduction reaction catalysts. *Nature Catal.* **2022**, *5*, 513−523.

(15) Bu, L. Z.; Zhang, N.; Guo, S. J.; Zhang, X.; Li, J.; Yao, J. L.; Wu, T.; Lu, G.; Ma, J. Y.; Su, D.; Huang, X. Q. Biaxially strained PtPb Pt core shell nanoplate boosts oxygen reduction catalysis. *Science* **2016**, *354*, 1410−1414.

(16) Han, B.; Carlton, C. E.; Kongkanand, A.; Kukreja, R. S.; Theobald, B. R.; Gan, L.; O'Malley, R.; Strasser, P.; Wagner, F. T.; Shao-Horn, Y. Record activity and stability of dealloyed bimetallic catalysts for proton exchange membrane fuel cells. *Energy Environ. Sci.* **2015**, *8*, 258−266.

(17) Nosberger, S.; Du, J.; Quinson, J.; Berner, E.; Zana, A.; Wiberg, G. K. H.; Arenz, M. The gas diffusion electrode setup as a testing platform for evaluating fuel cell catalysts: A comparative RDE-GDE study. *Electrochem. Sci. Adv.* **2022**, *3*, 1−12.

(18) Tovini, M. F.; Hartig-Weiß, A.; Gasteiger, H. A.; El-Sayed, H. A. The Discrepancy in Oxygen Evolution Reaction Catalyst Lifetime Explained: RDE vs MEA - Dynamicity within the Catalyst Layer Matters. *J. Electrochem. Soc.* **2021**, *168*, 014512.

(19) Knöppel, J.; Möckl, M.; Escalera-López, D.; Stojanovski, K.; Bierling, M.; Böhm, T.; Thiele, S.; Rzepka, M.; Cherevko, S. On the limitations in assessing stability of oxygen evolution catalysts using aqueous model electrochemical cells. *Nature Commun.* **2021**, *12*, 2231.

(20) Lazaridis, T.; Stuhmeier, B. M.; Gasteiger, H. A.; El-Sayed, H. A. Capabilities and limitations of rotating disk electrodes versus membrane electrode assemblies in the investigation of electrocatalysts. *Nature Catal.* **2022**, *5*, 363−373.

(21) Mo, S.; Du, L.; Huang, Z.; Chen, J.; Zhou, Y.; Wu, P.; Meng, L.; Wang, N.; Xing, L.; Zhao, M.; Yang, Y.; Tang, J.; Zou, Y.; Ye, S. Recent Advances on PEM Fuel Cells: From Key Materials to Membrane Electrode Assembly. *Electrochem. Energy Rev.* **2023**, *6*, 28.

(22) Fan, J.; Chen, M.; Zhao, Z.; Zhang, Z.; Ye, S.; Xu, S.; Wang, H.; Li, H. Bridging the gap between highly active oxygen reduction reaction catalysts and effective catalyst layers for proton exchange membrane fuel cells. *Nat. Energy* **2021**, *6*, 475−486.

(23) Cetinbas, F. C.; Ahluwalia, R. K.; Kariuki, N. N.; Myers, D. J. Agglomerates in Polymer Electrolyte Fuel Cell Electrodes: Part I. Structural Characterization. *J. Electrochem. Soc.* **2018**, *165*, F1051−F1058.

(24) Subbaraman, R.; Strmcnik, D.; Stamenkovic, V.; Markovic, N. M. Three Phase Interfaces at Electrified Metal-Solid Electrolyte Systems 1. Study of the Pt(hkl)-Nafion Interface. *J. Phys. Chem. C* **2010**, *114*, 8414−8422.

(25) Zeng, J.; Jean, D. I.; Ji, C.; Zou, S. In situ surface-enhanced Raman spectroscopic studies of nafion adsorption on Au and Pt electrodes. *Langmuir* **2012**, *28*, 957−964.

(26) Tada, M.; Iwasawa, Y. Fuel Cells by Advanced XAFS Techniques. In *XAFS Techniques for Catalysts, Nanomaterials and Surfaces*; Iwasawa, Y., Asakura, K., Tada, M., Eds.; Springer, 2016/2017; pp 335−349.

(27) Tada, M.; Murata, S.; Asakoka, T.; Hiroshima, K.; Okumura, K.; Tanida, H.; Uruga, T.; Nakanishi, H.; Matsumoto, S.; Inada, Y.; Nomura, M.; Iwasawa, Y. In Situ Time-Resolved Dynamic Surface Events on the Pt/C Cathode in a Fuel Cell under Operando Conditions. *Angew. Chem., Int. Ed.* **2007**, *46*, 4310−4315.

(28) Ishiguro, N.; Saida, T.; Uruga, T.; Nagamatsu, S.; Sekizawa, O.; Nitta, K.; Yamamoto, T.; Ohkoshi, S.; Iwasawa, Y.; Yokoyama, T.; Tada, M. Operando Time-Resolved X-ray Absorption Fine Structure Study for Surface Events on a Pt₃Co/C Cathode Catalyst in a Polymer Electrolyte Fuel Cell during Voltage-Operating Processes. *ACS Catal.* **2012**, *2*, 1319−1330.

(29) Nagamatsu, S.; Arai, T.; Yamamoto, M.; Ohkura, T.; Oyanagi, H.; Ishizaka, T.; Kawanami, H.; Uruga, T.; Tada, M.; Iwasawa, Y. Potential-Dependent Restructuring and Hysteresis in the Structural and Electronic Transformations of Pt/C, Au(Core)-Pt(Shell)/C, and Pd(Core)-Pt(Shell)/C Cathode Catalysts in Polymer Electrolyte Fuel Cells Characterized by in Situ X-ray Absorption Fine Structure. *J. Phys. Chem. C* **2013**, *117*, 13094−13107.

(30) Ishiguro, N.; Kityakarn, S.; Sekizawa, O.; Uruga, T.; Sasabe, T.; Nagasawa, K.; Yokoyama, T.; Tada, M. Rate Enhancements in Structural Transformations of Pt−Co and Pt−Ni Bimetallic Cathode Catalysts in Polymer Electrolyte Fuel Cells Studied by in Situ Time-Resolved X-ray Absorption Fine Structure. *J. Phys. Chem. C* **2014**, *118*, 15874−15883.

(31) Kaneko, T.; Samjeské, G.; Nagamatsu, S.; Higashi, K.; Sekizawa, O.; Takao, S.; Yamamoto, T.; Zhao, X.; Sakata, T.; Uruga, T.; Iwasawa, Y. Key Structural Kinetics for Carbon Effects on the Performance and Durability of Pt/Carbon Cathode Catalysts in Polymer Electrolyte Fuel Cells Characterized by *In Situ* Time-Resolved XAFS. *J. Phys. Chem. C* **2016**, *120*, 24250−24264.

(32) Ishiguro, N.; Saida, T.; Uruga, T.; Sekizawa, O.; Nagasawa, K.; Nitta, K.; Yamamoto, T.; Ohkoshi, S.; Yokoyama, T.; Tada, M. Structural kinetics of a Pt/C cathode catalyst with practical catalyst loading in an MEA for PEFC operating conditions studied by in situ time-resolved XAFS. *Phys. Chem. Chem. Phys.* **2013**, *15*, 18827−18834.

(33) Higashi, K.; Samjeské, G.; Takao, S.; Kaneko, T.; Sekizawa, O.; Uruga, T.; Iwasawa, Y. The Relationship between the Active Pt Fraction in a PEFC Pt/C Catalyst and the ECSA and Mass Activity during Start-Up/Shut-Down Degradation by in Situ Time-Resolved XAFS Technique. *J. Phys. Chem. C* **2017**, *121*, 22164−22177.

(34) Nagamatsu, S.; Takao, S.; Samjeské, G.; Nagasawa, K.; Sekizawa, O.; Kaneko, T.; Higashi, K.; Uruga, T.; Gayen, S.; Velaga, S.; Saniyal, M. K.; Iwasawa, Y. Structural and Electronic Transformations of Pt/C, Pd@Pt(1 ML)/C and Pd@Pt(2 ML)/C Cathode Catalysts in Polymer Electrolyte Fuel Cells during Potential-Step Operating Processes Characterized by In-situ Time-Resolved XAFS. *Surf. Sci.* **2016**, *648*, 100−113.

(35) Samjeské, G.; Kaneko, T.; Gunji, T.; Higashi, K.; Uruga, T.; Tada, M.; Iwasawa, Y. Feed Gas Exchange (Startup/Shutdown) Effects on Pt/C Cathode Electrocatalysis and Surface Pt-Oxide Behavior in Polymer Electrolyte Fuel Cell as Revealed by *In Situ* Real-Time XAFS and High-Resolution STEM. *Phys. Chem. Chem. Phys.* **2020**, *22*, 9424−9437.

(36) Gasteiger, H. A.; Kocha, S. S.; Sompalli, B.; Wagner, F. T. Activity benchmarks and requirements for Pt, Pt-alloy, and non-Pt oxygen reduction catalysts for PEMFCs. *Appl. Catal., B* **2005**, *56*, 9−35.

(37) Li, C.; Yu, K.; Bird, A.; Guo, F.; Ilavsky, J.; Liu, Y.; Cullen, D. A.; Kusoglu, A.; Weber, A. Z.; Ferreira, P. J.; et al. Unraveling the core of fuel cell performance: engineering the ionomer/catalyst interface. *Energy Environ. Sci.* **2023**, *16*, 2977−2990.

(38) Nagasawa, K.; Takao, S.; Higashi, K.; Nagamatsu, S.; Samjeské, G.; Imaizumi, Y.; Sekizawa, O.; Yamamoto, T.; Uruga, T.; Iwasawa, Y. Performance and Durability of Pt/C Cathode Catalysts with Different Kinds of Carbons for Polymer Electrolyte Fuel Cells Characterized by Electrochemical and *In-situ* XAFS Techniques. *Phys. Chem. Chem. Phys.* **2014**, *16*, 10075−10087.

(39) Shinozaki, K.; Morimoto, Y.; Pivovar, B. S.; Kocha, S. S. Suppression of oxygen reduction reaction activity on Pt-based electrocatalysts from ionomer incorporation. *J. Power Sources* **2016**, *325*, 745−751.

(40) Jinnouchi, R.; Kudo, K.; Kodama, K.; Kitano, N.; Suzuki, T.; Minami, S.; Shinozaki, K.; Hasegawa, N.; Shinohara, A. The role of oxygen-permeable ionomer for polymer electrolyte fuel cells. *Nat. Commun.* **2021**, *12*, 4956−4964.

(41) Ott, S.; Orfanidi, A.; Schmies, H.; Anke, B.; Nong, H. N.; Hubner, J.; Gernert, U.; Gliech, M.; Lerch, M.; Strasser, P. Ionomer distribution control in porous carbon-supported catalyst layers for high-power and low Pt-loaded proton exchange membrane fuel cells. *Nat. Mater.* **2020**, *19*, 77−85.

(42) Doo, G.; Yuk, S.; Lee, J. H.; Choi, S.; Lee, D.-H.; Lee, D. W.; Hyun, J.; Kwon, S. H.; Lee, S. G.; Kim, H.-T. Nano-scale control of the ionomer distribution by molecular masking of the Pt surface in PEMFCs. *J. Mater. Chem. A* **2020**, *8*, 13004−13013.

(43) Olbrich, W.; Kadyk, T.; Sauter, U.; Eikerling, M. Review— Wetting Phenomena in Catalyst Layers of PEM Fuel Cells: Novel Approaches for Modeling and Materials Research. *J. Electrochem. Soc.* **2022**, *169*, 054521.

(44) Eikerling, M.; Kornyshev, A. Electrochemical impedance of the cathode catalyst layer in polymer electrolyte fuel cells. *J. Electroanal. Chem.* **1999**, *475*, 107−123.

(45) Obermaier, M.; Bandarenka, A. S.; Lohri-Tymozhynsky, C. A comprehensive physical impedance model of polymer electrolyte fuel cell cathodes in oxygen-free atmosphere. *Sci. Reports* **2018**, *8*, 4933.

(46) Zhao, X.; Takao, S.; Yoshida, Y.; Kaneko, T.; Gunji, T.; Higashi, K.; Uruga, T.; Iwasawa, Y. Roles of structural defects in polycrystalline platinum nanowires for enhanced Oxygen Reduction Activity. *Appl. Catal. B: Environmental* **2023**, *324*, 122268.

(47) Li, K.; Li, X.; Huang, H.; Luo, L.; Li, X.; Yan, X.; Ma, C.; Si, R.; Yang, J.; Zeng, J. One-Nanometer-Thick PtNiRh Trimetallic Nano-wires with Enhanced Oxygen Reduction Electrocatalysis in Acid Media: Integrating Multiple Advantages into One Catalyst. *J. Am. Chem. Soc.* **2018**, *140*, 16159−16167.

(48) Newville, M.; Ravel, B.; Haskel, D.; Rehr, J. J.; Stern, E. A.; Yacoby, Y. Analysis of Multiple-Scattering XAFS Data Using Theoretical Standards. *Phys. B* **1995**, *208−209*, 154−156.

(49) Ravel, B.; Newville, M. ATHENA, ARTEMIS, HEPHAESTUS Data Analysis for X-ray Absorption Spectroscopy Using IFEFFIT. *J. Synchrotron Rad.* **2005**, *12*, 537−541.

(50) Rehr, J. J.; Albers, R. C. Theoretical Approaches to X-ray Absorption Fine Structure. *Rev. Mod. Phys.* **2000**, *72*, 621−654.